PHOTONICS Research

Dynamic multifunctional metasurfaces: an inverse design deep learning approach

Zhi-Dan Lei,[1,†] Yi-Duo Xu,[1,†] Cheng Lei,[1,3] Yan Zhao,[1,2,4] and Du Wang[1,*]

[1]The Institute of Technological Sciences, Wuhan University, Wuhan 430072, China
[2]College of Materials Science and Engineering, Sichuan University, Chengdu 610065, China
[3]e-mail: leicheng@whu.edu.cn
[4]e-mail: yan2000@whu.edu.cn
[†]These authors contributed equally to this paper.
*Corresponding author: wangdu@whu.edu.cn

Received 15 September 2023; revised 7 November 2023; accepted 12 November 2023; posted 14 November 2023 (Doc. ID 505991); published 22 December 2023

Optical metasurfaces (OMs) offer unprecedented control over electromagnetic waves, enabling advanced optical multiplexing. The emergence of deep learning has opened new avenues for designing OMs. However, existing deep learning methods for OMs primarily focus on forward design, which limits their design capabilities, lacks global optimization, and relies on prior knowledge. Additionally, most OMs are static, with fixed functionalities once processed. To overcome these limitations, we propose an inverse design deep learning method for dynamic OMs. Our approach comprises a forward prediction network and an inverse retrieval network. The forward prediction network establishes a mapping between meta-unit structure parameters and reflectance spectra. The inverse retrieval network generates a library of meta-unit structure parameters based on target requirements, enabling end-to-end design of OMs. By incorporating the dynamic tunability of the phase change material Sb_2Te_3 with inverse design deep learning, we achieve the design and verification of dynamic multifunctional OMs. Our results demonstrate OMs with multiple information channels and encryption capabilities that can realize multiple physical field optical modulation functions. When Sb_2Te_3 is in the amorphous state, near-field nano-printing based on meta-unit amplitude modulation is achieved for X-polarized incident light, while holographic imaging based on meta-unit phase modulation is realized for circularly polarized light. In the crystalline state, the encrypted information remains secure even with the correct polarization input, achieving double encryption. This research points towards ultra-compact, high-capacity, and highly secure information storage approaches.

https://doi.org/10.1364/PRJ.505991

1. INTRODUCTION

Optical metasurfaces (OMs) are two-dimensional structures composed of subwavelength meta-units, offering unique capabilities for manipulating optical wavefronts and enabling applications such as high-density optical storage and holography [1–3]. Unlike bulk metamaterials, OMs provide subwavelength resolution control over optical properties like amplitude, phase, polarization, and orbital angular momentum (OAM) [4–6]. Their arbitrary wavefront shaping capabilities have been extensively studied for imaging [7,8], holography [9–11], and nano-printing [12–14] applications, leading to the development of novel optical equipment such as focusing metalenses [15–17] and surface plasmonic coupling [6,18,19]. However, traditional OM design methods suffer from fixed functionalities and lack the ability to dynamically adjust, limiting their practical applications. To address this, embedding phase change materials (PCMs) in OMs has emerged as an approach to achieve dynamic functionality. PCMs are widely applied in the research field of "dynamic" OMs [20–24].

PCMs play a crucial role in the development of emerging non-volatile erasable optical storage technology [25–27]. Recent studies have demonstrated that PCMs are excellent active materials for achieving dynamic optical metasurfaces [21,28–30]. PCMs offer distinct advantages compared to other similar materials, as they exhibit significant changes in the optical refractive index between their crystalline and amorphous states. These unique properties include an exceptionally fast reversible switching speed in the nanosecond range and a phase change cycle lifetime of up to 10^{15} cycles [31]. "Dynamic" effects are mainly manifested by the aforementioned properties. Leveraging these remarkable characteristics, PCMs have shown great potential in various applications within the field of OMs, such as beam steering [32,33], optical

switches [34,35], optical computing [36,37], and photon spin–orbit interaction [38,39]. Among the typical PCMs, Sb-Te-based alloys have found widespread use in OMs research [22,40,41]. Specifically, Sb_2Te_3, owing to its growth-dominated crystallization and low melting point, offers a faster and less energy-intensive phase transition cycle compared to GST225 ($Ge_2Sb_2Te_5$), a typical PCM [42]. These advantageous properties of Sb_2Te_3 provide a solid foundation for its application in the field of OMs.

Deep learning, utilizing artificial neural networks (ANNs), is a remarkable methodology to effectively handle vast and complex data in OMs research [43–45]. Wei *et al.* proposed an iterative gradient optimization method based on machine learning, achieving excellent results in optical multiplexing for OMs holography [46]. Ma *et al.* demonstrated the accurate prediction of spectra and colors of OMs using deep learning neural networks [47]. However, it is worth noting that many studies, including these examples, have predominantly focused on forward modeling research of OMs [48–50]. In contrast, inverse design, which originated from the fluid dynamics community [51], offers valuable insights for addressing challenges like tuning dynamic degrees of freedom in OMs. Unlike traditional inverse design methods, deep learning network models can dynamically learn the intricate connections between meta-units and their corresponding optical responses from a training dataset in the design space. This adaptability enables the exploration of complex and multifunctional OMs. Furthermore, the combination of deep learning with genetic [52,53] and optimization algorithms [54,55] holds significant potential for enhancing the design process of such intricate and versatile OMs. In recent research, the application of inverse design deep learning has shown successful outcomes in the investigation of optical metalenses [56,57]. Nevertheless, it is noteworthy that the deep learning network architecture employed in these studies is fundamentally a forward network model, rather than an inverse neural network model. Additionally, these studies primarily focus on the design of a single parameter, which is insufficient for the comprehensive exploration of OMs with multiple parameters. In light of the rapid advancement of artificial intelligence (AI), the investigation of multifunctional OMs possessing multiple degrees of freedom has become an indispensable endeavor.

In this work, we propose a novel scheme for dynamic OMs using Sb_2Te_3 to achieve optical information. Deep learning serves as a mediator between the structural parameters of the meta-units and the desired functionalities of the OMs. Our approach, consisting of forward prediction and inverse retrieval networks, leverages deep learning and angular spectrum iterative optimization algorithms to accurately capture and reconstruct the statistical features of the multidimensional joint distribution between the meta-unit structures and their optical responses. This approach provides valuable insights into the design of multifunctional OMs.

2. DESIGN AND ALGORITHM

A. Design Principles of Multifunctional OMs

Figure 1 illustrates the method of using structured Sb_2Te_3 OMs for optical data encryption. In this approach, three distinct patterns are stored in three separate channels, each comprising individual meta-units of varying sizes and rotation angles. This fundamentally differs from existing functional

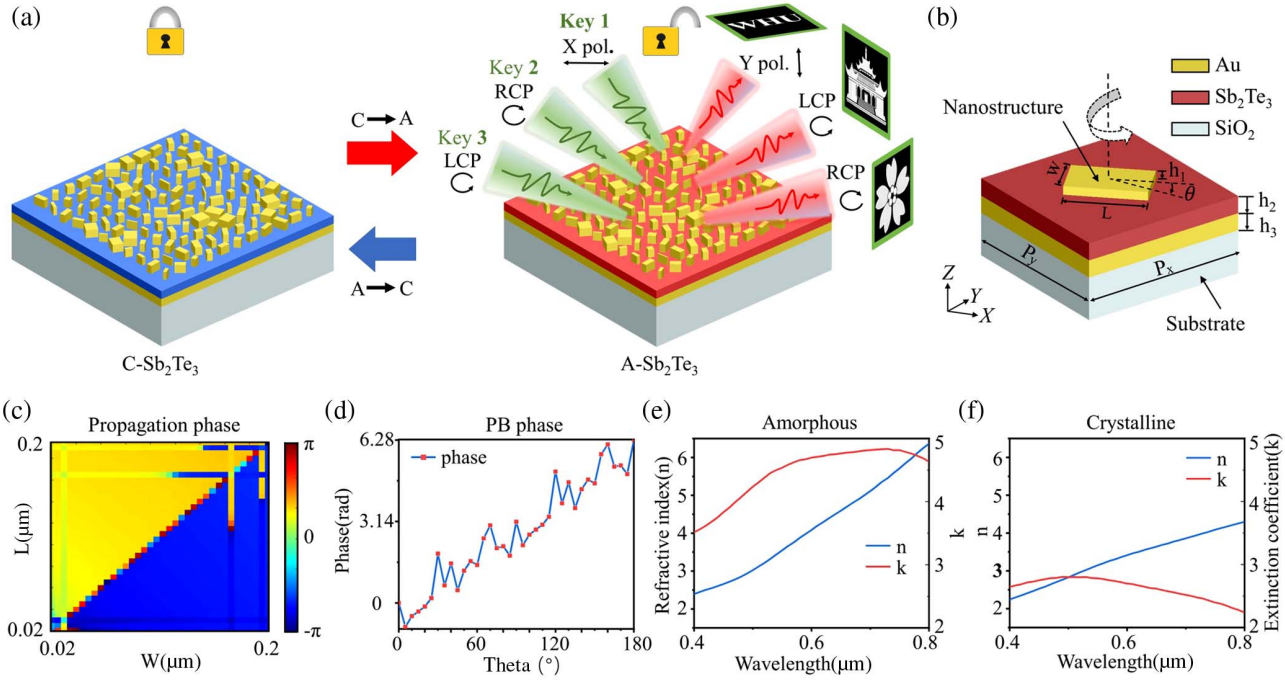

Fig. 1. Illustration of multifunctional OMs and the material optical properties. (a) Scheme of structured Sb_2Te_3 OMs for optical data encryption. (b) Structure design and related parameters of meta-unit. The periods P_x and P_y of meta-cell are 300 nm. The MIM layers' thicknesses h_1, h_2, and h_3 are 30, 90, and 130 nm, respectively. (c) Distribution of the propagation phase with the size of meta-unit. (d) Distribution of PB phases with the rotation angle of meta-unit. (e), (f) Refractive index n and extinction coefficient k of Sb_2Te_3 in (e) amorphous and (f) crystalline states [58].

OMs [59–61]. Each meta-unit serves as the fundamental working unit and contributes to the wavefront control of emitted light. Furthermore, unlike other design strategies involving ultra-compact solutions [62] or multi-layer design strategies [63,64] that require multiple wavefront manipulations, this proposed approach achieves active modulation of light's amplitude and phase using a single subwavelength-sized meta-unit. This enables independent functionalities and overcomes limitations such as signal crosstalk and information loss, resulting in an exceptionally high information storage density. Moreover, the dynamic tunability of Sb_2Te_3 allows for polymorphic, ultra-fast, reliable, non-volatile, and reversible optical information processing operations. Figure 1(a) demonstrates the encoding of information related to Wuhan University in the three separate channels. When the incident light's polarization state changes, the Sb_2Te_3 OMs modulate the light with different polarizations, revealing distinct stored information. Specifically, when the polarization of incident light is X-direction linearly polarized (LP), the "WHU" abbreviation becomes visible. A nano-printing process is employed in the near field, while the line patterns of the old library and the famous cherry blossoms of Wuhan University are encrypted in left-handed circular polarization (LCP) and right-handed circular polarization (RCP) in the far field, respectively.

The proposed multifunctional OMs are achieved by controlling the amplitude, phase, and polarization of reflected light through meta-units, as depicted in Fig. 1(b). The structural parameters of the meta-units, denoted by the parametric array $D = [L, W, \theta]$, are illustrated. The periods for the X- and Y-directions (P_x and P_y) are set to 300 nm. The meta-unit incorporates a metal–insulator–metal (MIM) plasmonic resonator, which enhances the optical response and enables precise phase control by adjusting the resonance conditions [65]. The thicknesses of MIM layers h_1, h_2, and h_3 are 30, 90, and 130 nm, respectively. The top resonator is designed as a coupled rectangular resonator. As shown in Fig. 1(b), each cuboid meta-unit acts as a half-wave plate capable of altering the polarization direction of light. This enables both amplitude modulation, achieved by controlling the rotation angle of the meta-unit in the near field following Malus' law, and phase modulation by changing the size and rotation angle in the far field. The cubic unit cell introduces different phase shifts, known as propagation phase, for orthogonal polarizations along the fast and slow axes. Figure 1(c) demonstrates the relationship between the size of the designed meta-units and the propagation phase, ranging from 0 to 2π. The geometric phase, also known as the Pancharatnam–Berry (PB) phase, is modulated by adjusting the rotation direction, as depicted in Fig. 1(d). The PB phase variation also spans 2π, enabling phase modulation. Thus, careful design enables complete wavefront control by manipulating both amplitude and phase in the spatial domain.

Most OMs are static and fixed in function once fabricated. However, in the context of AI development, dynamic OMs are crucial. Sb-Te-based alloys, as typical phase change materials, are excellent candidates for dynamic OMs. Sb_2Te_3, in particular, can rapidly and reproducibly switch between its amorphous (A-Sb_2Te_3) and crystalline (C-Sb_2Te_3) states when specific temperature or energy thresholds are reached. Figures 1(e) and 1(f) illustrate the refractive index n and extinction coefficient k of Sb_2Te_3 [58]. Information is stored in the amorphous Sb_2Te_3 structure, which becomes inaccessible when Sb_2Te_3 transitions into the crystalline state. In other words, when Sb_2Te_3 is in its crystalline state, the information related to Wuhan University remains completely hidden, achieving full encryption. Consequently, the proposed OMs offer benefits such as multifunctionality, high security, and information storage capacity, making them applicable to high-density information storage, compact image display, information encryption, and other related applications.

Compared to traditional design methods, deep learning methods offer several advantages in designing OMs, including automatic learning capability, flexibility, adaptability, large-scale design space exploration, accelerated design process, and integration of experimentation and simulation. In this work, inverse design deep learning models are employed for designing the proposed multifunctional OMs. The inverse design deep learning network consists of a forward predicting network model and an inverse retrieving network model. The design process for the multifunctional OMs is illustrated in Fig. 2.

The design process begins with defining specific design objectives, such as wavefront manipulation under various input conditions, as depicted in Fig. 2(a). These design objectives establish the desired intensity and phase distribution, which determine the desired optical response of each meta-unit. Solving the inverse problem of finding optimal geometric parameters for the OMs based on the desired optical response in multi-polarization scenarios is a challenging task. Additionally, determining whether a suitable meta-unit structure exists or how to better approximate the requirements for a fixed optical response is an even more difficult problem to solve. In Figs. 2(b) and 2(c), a retrieving network model is utilized to diversify the design of meta-units based on the desired intensity and phase, creating a meta-unit library for subsequent selection. The retrieving network model takes the desired intensity and phase as input and generates candidate meta-unit structures that satisfy the requirements. These generated meta-unit structures are then fed into a predicting network model to generate corresponding amplitude and phase responses, as shown in Fig. 2(d). The results of these optical responses are used to evaluate the design of the multifunctional OMs.

These two models are incorporated into the angular spectrum iterative optimization Gerchberg–Saxton (GS) algorithms to iteratively optimize and obtain the optimal solution. When integrating the GS algorithm into a deep learning model, the newly generated phase is mapped to the meta-unit geometry design. The prediction model calculates the deviation between the actual reflected spectra and the ideal values to reconstruct the target image. This deep learning model considers non-ideal phase retrieval by connecting the design domain and the physical domain, which is particularly crucial for multifunctional OM holograms that produce different images under various illumination conditions. Designing the desired optical response through meta-unit structure design can be challenging for many multifunctional OMs. However, the proposed closed-loop approach utilizes the entire design space to better approach the desired response and optimize the performance of the OMs.

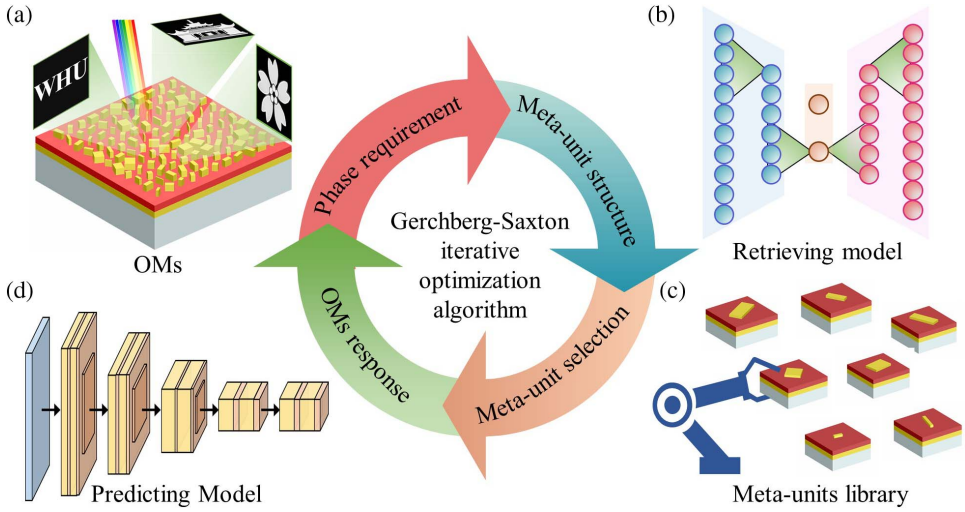

Fig. 2. Design process for the multifunctional OMs. (a) Proposed multifunctional OMs, (b) retrieving network model, (c) meta-unit library, and (d) predicting network model. These two deep learning network models are integrated into the GS iterative optimization algorithm, enabling bidirectional linkage between design objectives and OM geometric parameters.

B. Deep Learning Models for Inverse Design

To illustrate the inverse design process, we consider a single meta-unit as an example. The schematic diagram of the inverse design deep learning models is shown in Fig. 3. In this example, the information about Wuhan University is encoded using amorphous Sb_2Te_3, while the crystalline states are utilized for encryption purposes. We take into account the reflection electric field strength I and phase response φ of each meta-unit. The outputs in the X-direction are represented by (I_x, P_x), and the outputs in the Y-direction are represented by (I_y, P_y). The design parameters of a meta-unit are expressed in terms of the parametric array $(I, \varphi) = f(L, W, \theta)$, which plays a crucial role in the entire design space. In Fig. 3(a), each of the three parameters was sampled independently. The length L and width W were varied from 20 to 195 nm in 5 nm intervals, and the rotation angle θ was changed from 0° to 170° in 10°

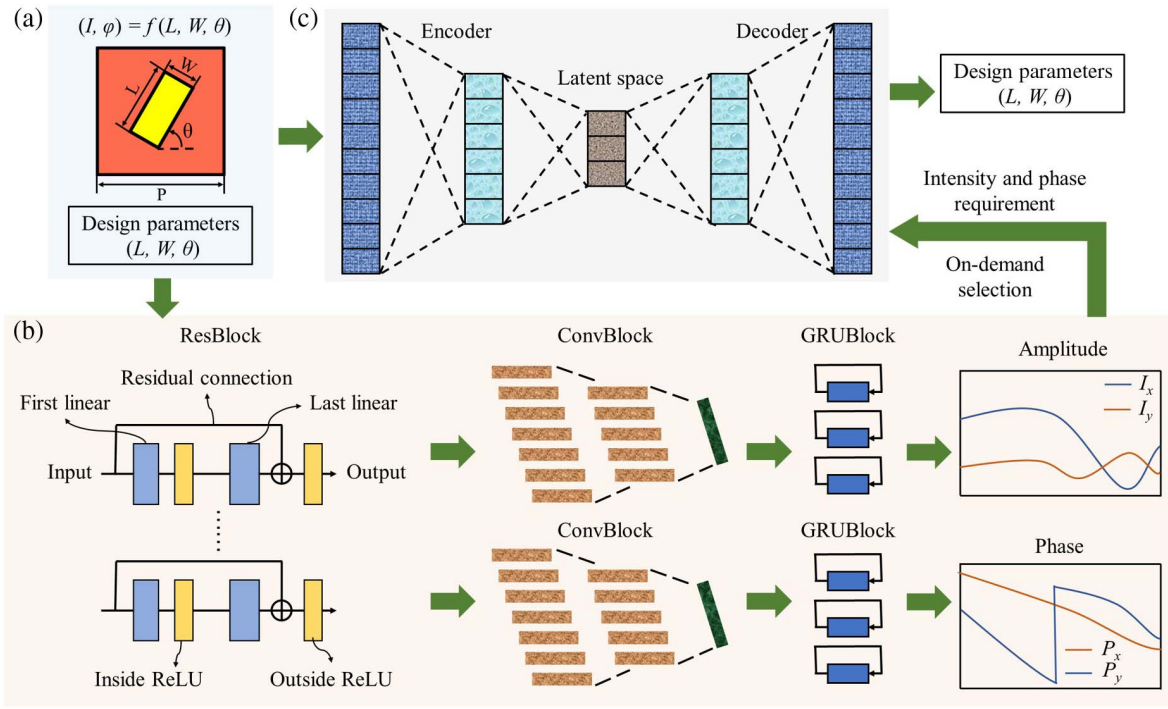

Fig. 3. Schematic diagram of the deep learning model for a single meta-unit design. (a) The design parameters of the meta-unit and the crystalline phase organization of Sb_2Te_3 are amorphous. (b) Predicting model for reflectance spectra and (c) retrieving model of the required intensity and phase. The forward prediction from design parameters to reflection spectra is fixed, whereas the on-demand inverse design process is characterized by uncertainty, thus ensuring the multiplicity of design outcomes.

Table 1. Detailed Configuration of the Predicting Model

Blocks	Layers	Size-In	Size-Out
ResBlock	Input	—	3 × 1
ResBlock	First linear	3 × 1	512 × 1
ResBlock	BasBlock1	512 × 1	1024 × 1
ResBlock	BasBlock2	1024 × 1	2048 × 1
ResBlock	BasBlock3	2048 × 1	2048 × 1
ResBlock	BasBlock4	2048 × 1	1024 × 1
ResBlock	BasBlock5	1024 × 1	512 × 1
ResBlock	BasBlock6	512 × 1	128 × 1
ConvBlock	ResConv1	128 × 1	3 × 128 × 512
ConvBlock	ResConv2	3 × 128 × 512	3 × 128 × 64
GRUBlock	GRU	3 × 128 × 64	3 × 128

intervals. A working wavelength of 520 nm is chosen, and the finite-difference-time-domain (FDTD) method is employed using the simulation package Ansys Lumerical 2021 R2 FDTD Solutions. Plane waves are used as the light source. The dielectric function of SiO_2 and Au is referenced from the experimental data of Palik [66] and Johnson and Christy [67], respectively.

The obtained reflectance spectra are then fed into the forward predicting network model, establishing a one-to-one mapping between the reflection spectra and the design parameters of the meta-unit. On the other hand, the inverse retrieving network model takes the desired intensity and phase as input and generates a one-to-many set of possible design parameters that satisfy the target requirements. In this study, a predicting model for reflectance spectra is proposed, leveraging the distinctive characteristics of different network architectures to enhance prediction performance, as depicted in Fig. 3(b).

First, the model incorporates the dense connection residual deep neural network block (ResBlock) as a crucial component. This block utilizes a dense connection structure, where the output of each layer is connected to the input of subsequent layers, facilitating efficient information flow. The residual connection mechanism allows the model to learn residual (difference) information by skipping layers, enabling better adaptation to complex features. This design enables the model to capture nonlinear relationships and subtle variations in the input data, thereby improving the accuracy of reflectance spectrum prediction. Second, convolutional blocks (ConvBlocks) are introduced to further extract features. The convolution operations effectively capture local patterns and structures in the input data by applying a series of filters. This process allows for the effective representation of spatial correlations, enhancing the model's ability to capture essential information. ConvBlocks typically consist of convolutional layers, activation functions, and pooling layers. The convolutional layers perform feature extraction, activation functions introduce nonlinearity, and pooling layers downsample the features. This structure efficiently reduces feature dimensions while preserving crucial spatial information, thereby improving the accuracy and robustness of spectrum prediction. Lastly, gated recurrent unit blocks (GRUBlocks) are incorporated to capture short-range and long-range dependencies between adjacent data points in the spectra. GRUBlocks utilize gate mechanisms such as resetting and updating gates to better control the flow of information, allowing for the effective capture of contextual dependencies in sequential data. Compared to traditional recurrent neural networks, GRUBlocks perform more effectively in capturing temporal relationships within reflectance spectra. The detailed configuration of the predicting model is provided in Table 1. This architecture effectively models the temporal relationships present in reflectance spectra. The mean squared error (MSE) function is used to calculate the loss between the input values and the validation values, which can be expressed as

$$\text{Loss} = \frac{1}{n}\sum_{i=1}^{n}\left(y_{\text{model}} - y_{\text{pre}}\right)^2, \tag{1}$$

where n is the sample size of the training set. y_{model} is the training or validating value. y_{pre} is the predicted value. Training loss was calculated using the Adam optimizer.

A proposed retrieving model aims to establish a one-to-many mapping between given optical requirements and potential design parameters, as depicted in Fig. 3(c). To achieve this, a deep generative model based on an encoder–decoder architecture is employed, which has demonstrated remarkable efficacy in similar research [68,69]. The encoder–decoder configuration facilitates the transformation of design parameters into a compressed latent space, enabling efficient representation and subsequent generation of diverse designs. During the training process, the encoder network acts as an information extractor, compressing the design parameters into a lower-dimensional latent space. This compression is achieved through a series of transformations and learned representations. By leveraging the power of neural networks, the encoder captures complex patterns and relationships within the input design parameters. To promote the generation of diverse designs, random sampling is performed from the resulting latent vectors, exploring various regions in the latent space. On the other hand, the decoder network functions as a generator, responsible for reconstructing the original design parameters from the sampled latent vectors and the given phase requirements. It takes the latent vectors and target requirements as inputs and generates predictions for the design parameters. Through a series of learned transformations and operations, the decoder learns to approximate the joint distribution of design parameters and latent vectors conditioned on the specified optical requirements. This allows the decoder to generate multiple design options that satisfy the intensity and phase constraints. To ensure the generalization capability of the retrieving model, a prior distribution on the latent space is imposed during training. This prior distribution incorporates prior knowledge or assumptions about the design space, guiding the decoder to focus on the most plausible regions of the latent space during generation. The detailed configuration of the retrieving model is shown in Table 2.

The Kullback–Leibler (KL) divergence is utilized to measure the similarity between the reconstruction results and the training sample distribution, which can be described as

$$D_{\text{KL}}(p\|q) = -\sum_{x} p(x)\log\frac{q(x)}{p(x)}, \tag{2}$$

Table 2. Detailed Configuration of the Retrieving Model

Blocks	Layers	Size-In	Size-Out
Encoder	Input	$(3+6)\times 1$	1000×1
Encoder	First linear	1000×1	1000×1
Encoder	Second linear	1000×1	800×1
Encoder	Third linear	800×1	400×1
Encoder	Fourth linear	400×1	200×1
Encoder	Fifth linear	200×1	128×1
Encoder	Output	128×1	$(9+9)\times 1$
Decoder	Input	$(9+6)\times 1$	128×1
Decoder	First linear	128×1	200×1
Decoder	Second linear	200×1	400×1
Decoder	Third linear	400×1	800×1
Decoder	Fourth linear	800×1	1000×1
Decoder	Fifth linear	1000×1	1000×1
Decoder	Output	1000×1	3×1

where p or q is a random variable. x is a random variable value. $p(x)$ and $q(x)$ denote the probability distribution of x.

3. RESULTS AND DISCUSSION

A. Performance Evaluation of Deep Learning Models

The proposed deep learning model possesses prediction and retrieval capabilities, allowing it to capture the characteristics of design parameters and corresponding reflection spectra. It eliminates the need for empirical human intervention and mitigates adverse effects caused by global optimization or specific device functionalities, enabling the achievement of complex multifunctional OMs. The rate between the training set and validation set is 7:3 [70–72]. Figure 4(a) presents the deep learning dataset, where each meta-unit corresponds to a half-wave plate. When the incident light is X-polarized, the polarization of the output light is Y-polarized, so the value of I_x is close to zero. The reflection phases P_x and P_y of each CP both cover a range of 2π, indicating that the samples meet the design requirements for phase-modulating multifunctional OMs.

The performance of the proposed deep learning model is then analyzed. First, the deep learning dataset's consistency is evaluated using kernel density estimation (KDE) to compute mutual information among the training, testing, and validation datasets. Figure 4(b) demonstrates good consistency in the distributions of the training set, testing set, and validation set, indicating that the model can reproduce the statistical features of multidimensional reflectance spectra. Additionally, the correlation of the data is analyzed [Fig. 4(c)], revealing that the three parameters are uncorrelated, further supporting the model's ability to reproduce the statistical characteristics of reflectance spectra. The forward predicting model is trained using the input datasets. Figure 4(d) illustrates the training results for the three polarizations, showing that the training errors remain well below 0.001 as the epoch increases. Although the values are close to zero, resulting in slightly worse training and validating results, the loss stabilizes below 0.0005. These results indicate that the forward predicting model performs well.

To obtain the desired phase distribution for specific multifunctional OMs, the GS algorithm is combined, and the obtained phase distribution is then input into the retrieving network model to determine the meta-unit distribution. The distribution of the training and validation sets is validated in Fig. 5(a), demonstrating that both sets follow the same distribution. Additionally, to evaluate the performance of the retrieving network, 20 samples are randomly selected. Figure 5(b) displays scatterplots showing a good match among the real, predicted, and generated values for these 20 samples. To provide a more precise assessment of the retrieving network model's effectiveness, the values are quantitatively analyzed using Pearson correlations, as shown in Fig. 5(c). The symbol "*" indicates a highly significant correlation between the two variables. It can be observed that there is a strong correlation among the real, predicted, and generated values for each polarization state, demonstrating the reliability of our model. Moreover, the data for each polarization state are not correlated with each other, further supporting the feasibility and rationalization of our three independent channels for multifunctional OMs.

The reconstruction performance of the retrieval network is assessed using three sample images of size 100×100 pixels. The retrieval network effectively regenerates the intensity and phase information of the target pattern and combines them to generate a reconstructed pattern, as depicted in Fig. 6. The reconstructed intensity and phase map closely resemble the target phase and pattern, providing further evidence of the reliability of our deep learning models.

B. Nano-printing and Holography of Multifunctional Dynamic OMs

By manipulating the state transition of Sb_2Te_3, we can achieve dynamic multifunctional OMs suitable for nano-printing and holographic imaging. In this study, we have developed a multifunctional OM device designed to operate at a wavelength of 520 nm, supporting various polarizations, including LP in the X-direction (X), LCP, and RCP. The OMs consist of 100×100 pixels, covering a total area of $31.2\ \mu m\times 31.2\ \mu m$. The simulation results presented in Fig. 7 were obtained using Lumerical FDTD Solutions simulation, and holography was calculated using the Fraunhofer diffraction integral. The intensity of the image across the three channels is normalized [31]. As depicted in Fig. 7, when the Sb_2Te_3 state is in the amorphous phase, we observe one near-field nano-printing image and two far-field holograms in three distinct emitting light channels. Specifically, when the incident light is linearly polarized in the X-direction, the abbreviation "WHU" (representing Wuhan University) is printed in the near field through amplitude modulation of meta-units. Under LCP and RCP, the far-field holograms display line patterns from an old library and the famous cherry blossoms of Wuhan University, respectively, achieved through phase modulation of meta-units. It is important to note that the encoded information in all three channels is polarization-dependent and can only be decrypted under specific polarization conditions. When the state of Sb_2Te_3 transitions to the crystalline, even with the correct decoding information inputted, the encoded information remains invisible, providing double the information encryption. The figure clearly illustrates that under the amorphous state, the simulation results closely match the original target images, demonstrating the feasibility of our proposed design approach.

The results of nano-printing and holograms using dynamic multifunctional OMs demonstrate the excellent capabilities of

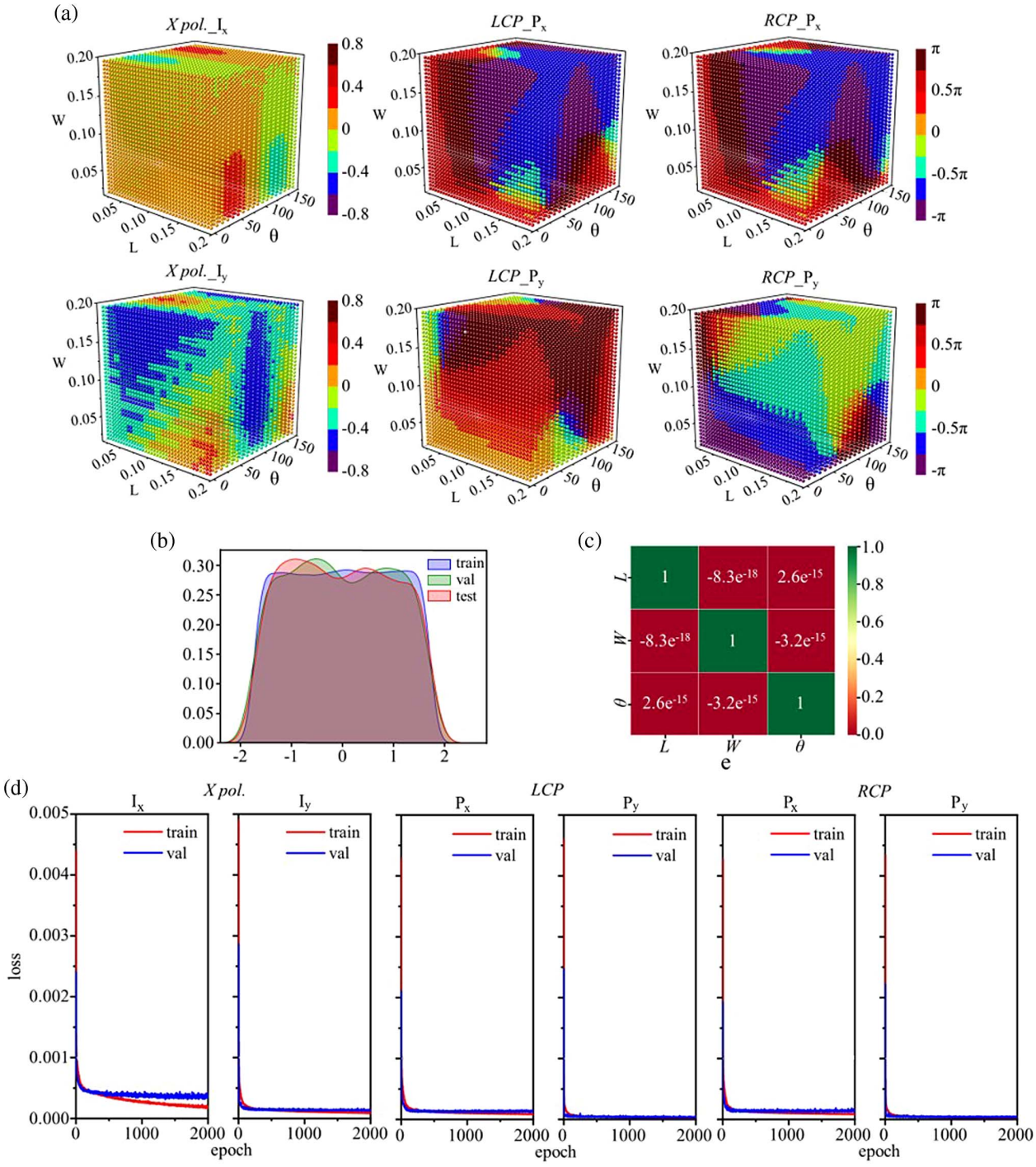

Fig. 4. Training results of the forward predicting network model. (a) Datasets for the forward deep learning network. The total data quantity of each cuboid is 23,328. (b) Distribution of datasets. (c) Correlation analysis of parameters. (d) Training and validation loss of *X* polarization, LCP, and RCP at wavelength of 520 nm.

the PCM-based Sb_2Te_3 OMs in achieving full wavefront modulation in both amplitude and phase domains, offering dynamic versatility. This design holds significant potential for various applications in optical information transmission and encryption. In addition, the designed dynamic multifunctional OMs incorporate multiple encryption regimes, enhancing their security features. The three independent target information channels embedded within a single OM can only be accessed under specific polarization conditions, effectively using the decoded polarization state as a security key. Additionally, the state transition of the PCM can be utilized for information encryption. When optical information is encoded in one state of the PCM, it becomes inaccessible in another state. Hence, our proposed dynamic multifunctional OMs provide a multi-mechanism approach to information encryption, significantly augmenting the security of stored information.

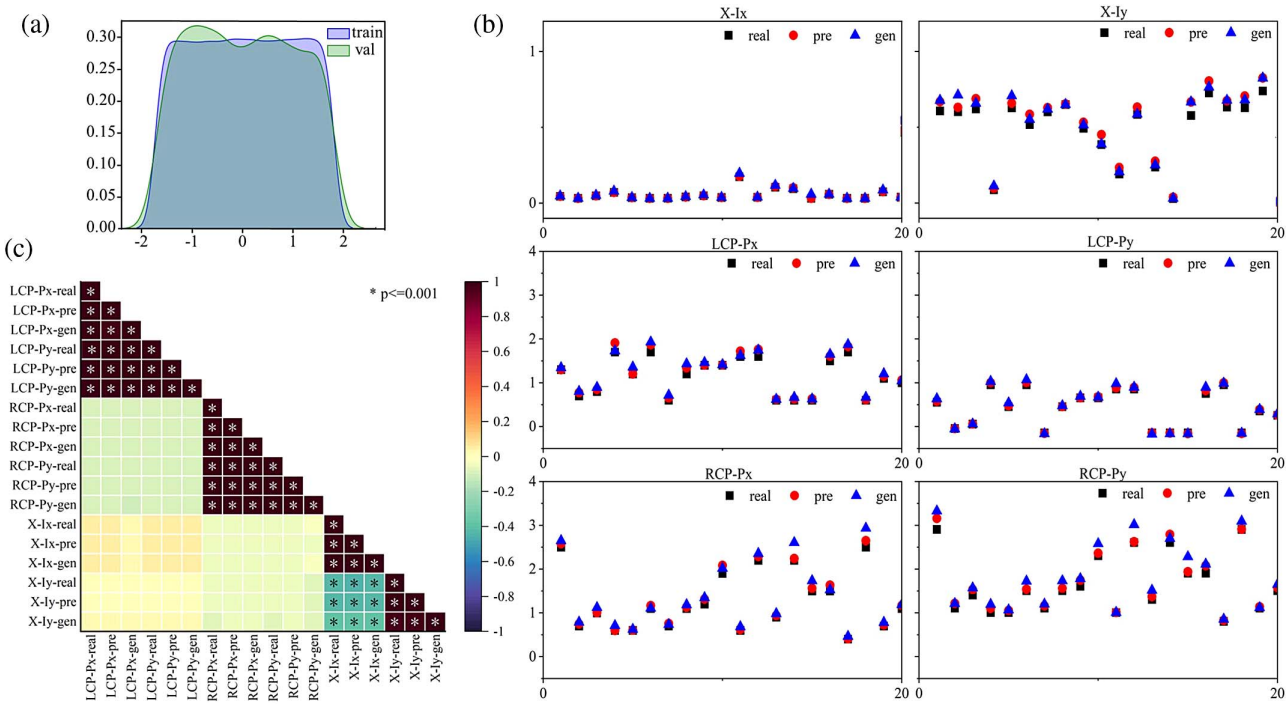

Fig. 5. Training results of the retrieving model. (a) Distribution of datasets and (b) correspondence among the real, predicted, and generated values of X polarization, LCP, and RCP. The black plot represents the target values, the red plot represents the predicted values, and the blue plot represents the generated values. (c) Pearson correlations among the real, predicted, and generated values for each polarization.

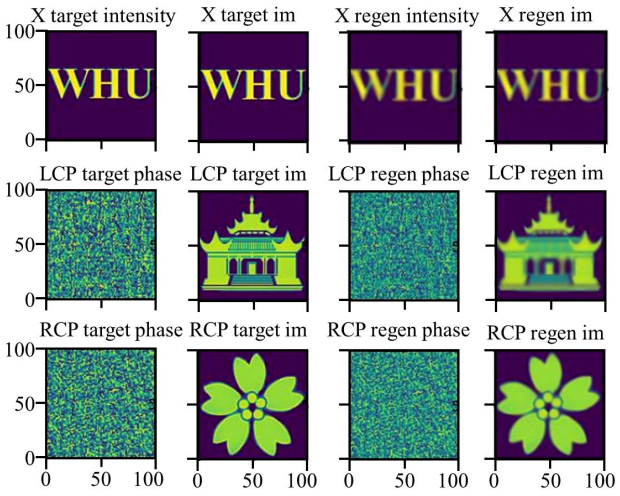

Fig. 6. Intensity and phase regeneration results of the retrieving model. Comparison images among the target phase, target image, reconstructed phase, and reconstructed image for each polarization state.

C. Discussion

This study proposes a design methodology for dynamic multifunctional OMs using inverse design deep learning, showcasing its effectiveness through simulations. The dynamism of the OMs is achieved by manipulating the state of Sb_2Te_3. When Sb_2Te_3 is in the amorphous state, the encrypted information can be accessed with the correct key. However, in the crystalline state, even with the correct key, the stored information remains inaccessible. Alternatively, manipulating the ratio between crystalline and amorphous states of PCMs can yield a more pronounced and visually captivating dynamic effect. For example, the display states of the nano-printing and hologram can be controlled by adjusting the crystallization level of the PCM, such as setting the crystallinity levels to 0%, 50%, and 100%. This approach also enhances multichannel multiplexing in multifunctional OMs. Importantly, the proposed design methodology is not limited to Sb_2Te_3 and can be applied to other materials with different control mechanisms to achieve dynamic effects. Additionally, the proposed multichannel OMs can enhance information encryption by incorporating different wavelengths, polarizations, and other parameters.

The deep learning network model employed in this research serves as a generalized design approach, not restricted to the type of meta-unit discussed in this paper. By adjusting the model of the meta-unit, the design of other multifunctional OMs such as metalenses and Pancharatnam–Berry (PB) OMs can be realized. Moreover, apart from the non-gradient optimization GS phase retrieval algorithm, the proposed deep learning network models can be flexibly combined with various algorithms, including gradient-based optimization algorithms and other non-gradient iterative optimization algorithms. Furthermore, the paper utilizes X-direction linear polarization as a primary focus, yet it is worth noting that linear polarization in alternative directions can also be employed. For instance, linear polarization with a specific tilt angle allows for the simultaneous presence of non-zero components in both X- and Y-directions, potentially leading to improved training accuracy.

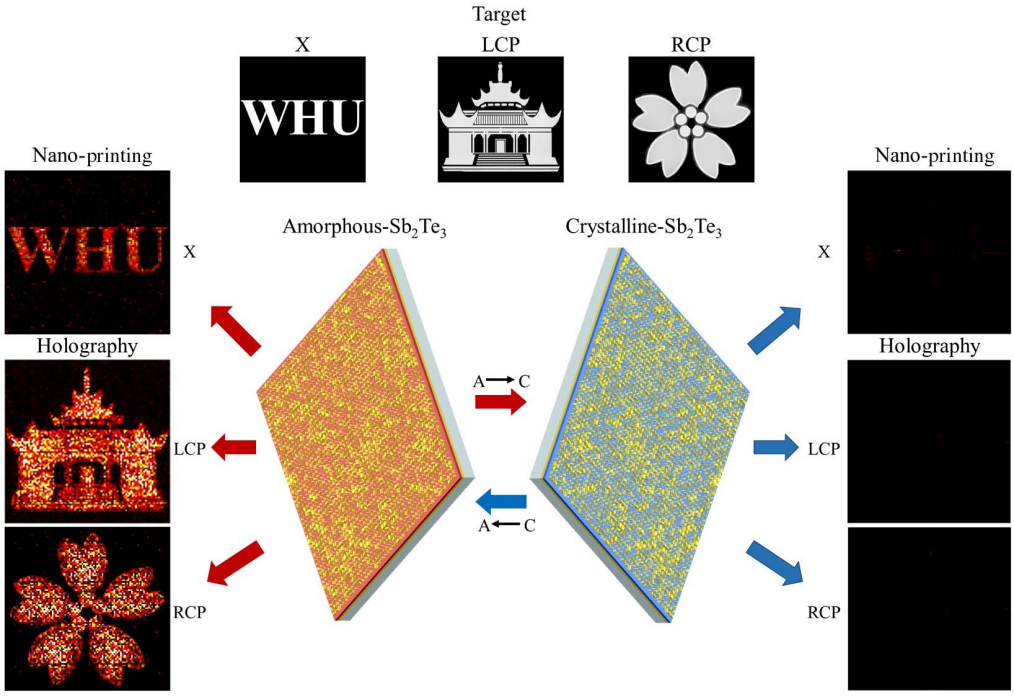

Fig. 7. Target image and calculated results of multifunctional OMs under *X* polarization, LCP, and RCP. These calculated results are obtained through the combination of simulation results and the utilization of Fraunhofer diffraction integrals.

Similarly, the substitution of orthogonal circular polarization with orthogonal elliptical polarization can yield a comparable effect.

To demonstrate the feasibility of the proposed approach, target images with a pixel size of 100 × 100 pixels are selected. In practical applications, the pattern size can be adjusted according to specific requirements. As the size expands, the resolution of the regenerated image can be further increased, albeit at the cost of computational resources and time. In the context of designing large-sized OMs, several relevant studies have suggested the utilization of image segmentation and integrated OMs [73–77] as effective approaches for achieving continuous design of oversized OMs. Consequently, our proposed method not only caters to the requirements of designing complex OMs on a large scale but also holds promise for various other applications, including optical storage, laser fabrication, information processing, and optical communications. It is important to note that the quality of the designed target hologram is primarily influenced by the localized surface plasmon resonance (LSPR) between the meta-units. Unlike single-sized PB OMs, the impact of LSPR is challenging to eliminate for improving image quality. Nevertheless, the results indicate that our designed multifunctional OMs can still achieve independent multichannel operations.

4. CONCLUSIONS

This work proposes a dynamic multifunctional OMs design method based on inverse design deep learning. It combines deep learning with phase change materials (PCMs) to achieve dynamic nano-printing and holographic imaging of three independent polarization channels. The design method consists of a forward prediction network and an inverse retrieval network. The forward prediction network establishes a mapping between meta-unit design parameters and reflected light intensity and phase, with training and validation errors below 0.005 in all polarizations. The inverse retrieval network, combined with the angular spectrum iterative GS algorithm, generates meta-unit structure parameters based on target light intensity and phase inputs. The effectiveness of the retrieval network is assessed using the Pearson correlation coefficient, showing significant correlations with *p*-values below 0.001 for light intensity and phase in each polarization. The dynamics of the OMs are achieved through material selection, utilizing the tunability of Sb_2Te_3. The designed OMs, generated by inverse design deep learning, demonstrate dynamic multifunctionality in FDTD simulations. For example, when Sb_2Te_3 is amorphous, the OMs display the abbreviation "WHU," line patterns of an old library, and cherry blossoms under specific polarizations. Transitioning to the crystalline state enables information encryption even with the correct decoding information. This embedded inverse design deep learning model combined with PCM offers a new approach for dynamic multifunctional OMs. The proposed OMs exhibit multifunctionality, compactness, high information capacity, and security advantages, making them promising for active OM devices, information storage, and encryption applications.

Funding. National Key Research and Development Program of China (2023YFB4603803); National Natural Science Foundation of China (62075200, 12374295, 22273069); Key R&D Program of Hubei (2021BAA173); Fundamental Research Funds for the Central Universities (2042023kf0113, 2042022gf0004).

Disclosures. The authors declare no conflicts of interest.

Data Availability. Data underlying the results presented in this paper are not publicly available at this time but may be obtained from the authors upon reasonable request.

REFERENCES

1. C. L. Holloway, E. F. Kuester, and J. A. Gordon, *et al.*, "An overview of the theory and applications of metasurfaces: the two-dimensional equivalents of metamaterials," IEEE Antennas Propag. Mag. **54**, 10–35 (2012).
2. T. J. Cui, S. Liu, and L. Zhang, "Information metamaterials and metasurfaces," J. Mater. Chem. C **5**, 3644–3668 (2017).
3. S. Chang, X. Guo, and X. Ni, "Optical metasurfaces: progress and applications," Annu. Rev. Mater. Res. **48**, 279–302 (2018).
4. H. H. Hsiao, C. H. Chu, and D. P. Tsai, "Fundamentals and applications of metasurfaces," Small Methods **1**, 1600064 (2017).
5. F. Zhang, M. Pu, and P. Gao, *et al.*, "Simultaneous full-color printing and holography enabled by centimeter-scale plasmonic metasurfaces," Adv. Sci. **7**, 1903156 (2020).
6. F. Dong and W. Chu, "Multichannel-independent information encoding with optical metasurfaces," Adv. Mater. **31**, 1804921 (2019).
7. M. Khorasaninejad, W. T. Chen, and R. C. Devlin, *et al.*, "Metalenses at visible wavelengths: diffraction-limited focusing and subwavelength resolution imaging," Science **352**, 1190–1194 (2016).
8. K. H. Dou, X. Xie, and M. B. Pu, *et al.*, "Off-axis multi-wavelength dispersion controlling metalens for multi-color imaging," Opto-Electronic Adv. **3**, 19000501 (2020).
9. H. Ren, X. Fang, and J. Jang, *et al.*, "Complex-amplitude metasurface-based orbital angular momentum holography in momentum space," Nat. Nanotechnol. **15**, 948–955 (2020).
10. H. Gao, X. Fan, and W. Xiong, *et al.*, "Recent advances in optical dynamic meta-holography," Opto-Electronic Adv. **4**, 210030 (2021).
11. G. Zheng, H. Mühlenbernd, and M. Kenney, *et al.*, "Metasurface holograms reaching 80% efficiency," Nat. Nanotechnol. **10**, 308–312 (2015).
12. K. Chen, J. Li, and G. Zhu, *et al.*, "Phase-assisted angular-multiplexing nanoprinting based on the Jacobi-Anger expansion," Opt. Express **30**, 46552–46559 (2022).
13. Q. Dai, G. Zhu, and W. Zhang, *et al.*, "Dual-channel anticounterfeiting color-nanoprinting with a single-size nanostructured metasurface," Opt. Express **30**, 33574–33587 (2022).
14. R. Fu, K. Chen, and Z. Li, *et al.*, "Metasurface-based nanoprinting: principle, design and advances," Opto-Electronic Sci. **1**, 220011 (2022).
15. S. Luan, F. Peng, and G. Zheng, *et al.*, "High-speed, large-area and high-precision fabrication of aspheric micro-lens array based on 12-bit direct laser writing lithography," Light Adv. Manuf. **3**, 47 (2022).
16. G. Yoon, K. Kim, and S. U. Kim, *et al.*, "Printable nanocomposite metalens for high-contrast near-infrared imaging," ACS Nano **15**, 698–706 (2021).
17. G. Yoon, K. Kim, and D. Huh, *et al.*, "Single-step manufacturing of hierarchical dielectric metalens in the visible," Nat. Commun. **11**, 2268 (2020).
18. A. M. Selman and M. J. Kadhim, "Fabrication of GaN nanocrystalline thin films Schottky metal-semiconductor-metal ultraviolet photodetectors," Optik **265**, 169418 (2022).
19. Y. Liu, L. Gui, and K. Xu, "Enhancement of second-harmonic generation from Fano plasmonic metasurfaces by introducing structural asymmetries," Opt. Express **30**, 42440–42453 (2022).
20. S. Zhuo, Y. Li, and A. Zhao, *et al.*, "Dynamic transmissive metasurface for broadband phase-only modulation based on phase-change materials," Laser Photonics Rev. **17**, 2200403 (2023).
21. F. Ding, Y. Yang, and S. I. Bozhevolnyi, "Dynamic metasurfaces using phase-change chalcogenides," Adv. Opt. Mater. **7**, 1801709 (2019).
22. S. Abdollahramezani, O. Hemmatyar, and M. Taghinejad, *et al.*, "Dynamic hybrid metasurfaces," Nano Lett. **21**, 1238–1245 (2021).
23. A. Forouzmand and H. Mosallaei, "Dynamic beam control via Mie-resonance based phase-change metasurface: a theoretical investigation," Opt. Express **26**, 17948–17963 (2018).
24. T. Tang, K. He, and L. Bi, *et al.*, "Dynamic beam scanning metasurface with high reflectivity and independent phase control based on phase change materials," Opt. Laser Technol. **156**, 108543 (2022).
25. K. Xu, X. Miao, and M. Xu, "The structure of phase-change chalcogenides and their high-pressure behavior," Phys. Status Solidi - RRL **13**, 1800506 (2019).
26. M. Wuttig and N. Yamada, "Phase-change materials for rewriteable data storage," Nat. Mater. **6**, 824–832 (2007).
27. X. P. Wang, X. Bin Li, and N. K. Chen, *et al.*, "Phase-change-memory process at the limit: a proposal for utilizing monolayer Sb_2Te_3," Adv. Sci. **8**, 2004185 (2021).
28. M. Wuttig, H. Bhaskaran, and T. Taubner, "Phase-change materials for non-volatile photonic applications," Nat. Photonics **11**, 465–476 (2017).
29. S. Xiao, T. Wang, and T. Liu, *et al.*, "Active metamaterials and metadevices: a review," J. Phys. D **53**, 503002 (2020).
30. A. Mandal, Y. Cui, and L. McRae, *et al.*, "Reconfigurable chalcogenide phase change metamaterials: a material, device, and fabrication perspective," J. Phys. Photonics **3**, 022005 (2021).
31. T. Liu, Z. Han, and J. Duan, *et al.*, "Phase-change metasurfaces for dynamic image display and information encryption," Phys. Rev. Appl. **18**, 044078 (2022).
32. Y. Zhang, C. Fowler, and J. Liang, *et al.*, "Electrically reconfigurable non-volatile metasurface using low-loss optical phase-change material," Nat. Nanotechnol. **16**, 661–666 (2021).
33. C. R. de Galarreta, A. M. Alexeev, and Y. Y. Au, *et al.*, "Nonvolatile reconfigurable phase-change metadevices for beam steering in the near infrared," Adv. Funct. Mater. **28**, 1704993 (2018).
34. P. Guo, M. S. Weimer, and J. D. Emery, *et al.*, "Conformal coating of a phase change material on ordered plasmonic nanorod arrays for broadband all-optical switching," ACS Nano **11**, 693–701 (2017).
35. P. Li, X. Yang, and T. W. W. Maß, *et al.*, "Reversible optical switching of highly confined phonon-polaritons with an ultrathin phase-change material," Nat. Mater. **15**, 870–875 (2016).
36. Z. Cheng, C. Ríos, and N. Youngblood, *et al.*, "Device-level photonic memories and logic applications using phase-change materials," Adv. Mater. **30**, 1802435 (2018).
37. C. Wu, H. Yu, and S. Lee, *et al.*, "Programmable phase-change metasurfaces on waveguides for multimode photonic convolutional neural network," Nat. Commun. **12**, 96 (2021).
38. T. Tang, Y. Tang, and L. Bi, *et al.*, "Highly sensitive real-time detection of phase change process based on photonic spin Hall effect," Appl. Phys. Lett. **120**, 191105 (2022).
39. X. Luo, X. Li, and M. Pu, *et al.*, "Symmetric and asymmetric photonic spin-orbit interaction in metasurfaces," Prog. Quantum Electron. **79**, 100344 (2021).
40. L. Kang, R. P. Jenkins, and D. H. Werner, "Recent progress in active optical metasurfaces," Adv. Opt. Mater. **7**, 1801813 (2019).
41. K. Guo, X. Li, and H. Ai, *et al.*, "Tunable oriented mid-infrared wave based on metasurface with phase change material of GST," Results Phys. **34**, 105269 (2022).
42. S. C. Tiwari, R. K. Kalia, and A. Nakano, *et al.*, "Photoexcitation induced ultrafast nonthermal amorphization in Sb_2Te_3," J. Phys. Chem. Lett. **11**, 10242–10249 (2020).
43. L. Li, H. Ruan, and C. Liu, *et al.*, "Machine-learning reprogrammable metasurface imager," Nat. Commun. **10**, 1082 (2019).
44. L. Xu, M. Rahmani, and Y. Ma, *et al.*, "Enhanced light-matter interactions in dielectric nanostructures via machine-learning approach," Adv. Photonics **2**, 026003 (2020).
45. M. V. Zhelyeznyakov, S. Brunton, and A. Majumdar, "Deep learning to accelerate scatterer-to-field mapping for inverse design of dielectric metasurfaces," ACS Photonics **8**, 481–488 (2021).
46. Q. Wei, L. Huang, and R. Zhao, *et al.*, "Rotational multiplexing method based on cascaded metasurface holography," Adv. Opt. Mater. **10**, 2102166 (2022).
47. H. Ma, N. Dalloz, and A. Habrard, *et al.*, "Predicting laser-induced colors of random plasmonic metasurfaces and optimizing image multiplexing using deep learning," ACS Nano **16**, 9410–9419 (2022).

48. Z. Lei, D. Yang, and Y. Xu, *et al.*, "Achieving ultra-high-density two-dimensional optical storage through angle resolved LSPR arrays: a case study of square array," Opt. Commun. **546**, 129798 (2023).
49. L. Song, D. Yang, and Z. Lei, *et al.*, "A reflectivity enhanced 3D optical storage nanostructure," Materials **16**, 2668 (2023).
50. D. Yang, Z. Lei, and L. Li, *et al.*, "High optical storage density using three-dimensional hybrid nanostructures based on machine learning," Opt. Lasers Eng. **161**, 107347 (2023).
51. A. Jameson, L. Martinelli, and N. A. Pierce, "Optimum aerodynamic design using the Navier-Stokes equations," Theor. Comput. Fluid Dyn. **10**, 213–237 (1998).
52. G. Wu, L. Si, and H. Xu, *et al.*, "Phase-to-pattern inverse design for a fast realization of a functional metasurface by combining a deep neural network and a genetic algorithm," Opt. Express **30**, 45612–45623 (2022).
53. Y. Teng, C. Li, and S. Li, *et al.*, "Efficient design method for terahertz broadband metasurface patterns via deep learning," Opt. Laser Technol. **160**, 109058 (2023).
54. W. Ji, J. Chang, and H. X. Xu, *et al.*, "Recent advances in metasurface design and quantum optics applications with machine learning, physics-informed neural networks, and topology optimization methods," Light Sci. Appl. **12**, 169 (2023).
55. S. An, C. Fowler, and B. Zheng, *et al.*, "A deep learning approach for objective-driven all-dielectric metasurface design," ACS Photonics **6**, 3196–3207 (2019).
56. J. He, Z. Guo, and Y. Zhang, *et al.*, "Physics-model-based neural networks for inverse design of binary phase planar diffractive lenses," Opt. Lett. **48**, 1474–1477 (2023).
57. Y. Zhu, Y. Chen, and L. Dal Negro, "Design of ultracompact broadband focusing spectrometers based on diffractive optical networks," Opt. Lett. **47**, 6309–6312 (2022).
58. A. Mandal, Y. Cui, and L. Mcrae, *et al.*, "Reconfigurable chalcogenide phase change metamaterials : a material, device, and fabrication perspective," J. Phys. Photonics **3**, 022005 (2021).
59. J. Li, S. Kamin, and G. Zheng, *et al.*, "Addressable metasurfaces for dynamic holography and optical information encryption," Sci. Adv. **4**, eaar6768 (2018).
60. B. Dong, R. Zhao, and Q. Wei, *et al.*, "Terahertz switchable VO_2-Au hybrid active metasurface holographic encryption," Opt. Express **30**, 20750–20761 (2022).
61. S. Jia, J. Liu, and A. U. R. Khalid, *et al.*, "Composite nanostructured design for dynamic control of metasurface holograms," J. Opt. Soc. Am. B **37**, 658–664 (2020).
62. B. Liu, W. Zhao, and Y. Jiang, "Apparent negative reflection with the gradient acoustic metasurface by integrating supercell periodicity into the generalized law of reflection," Sci. Rep. **6**, 38314 (2016).
63. J. H. Song, J. van de Groep, and S. J. Kim, *et al.*, "Non-local metasurfaces for spectrally decoupled wavefront manipulation and eye tracking," Nat. Nanotechnol. **16**, 1224–1230 (2021).
64. C. Wang, H. X. Xu, and Y. Wang, *et al.*, "Reconfigurable transmissive metasurface synergizing dynamic and geometric phase for versatile polarization and wavefront manipulations," Mater. Des. **225**, 111445 (2023).
65. C. Qu, S. Ma, and J. Hao, *et al.*, "Tailor the functionalities of metasurfaces based on a complete phase diagram," Phys. Rev. Lett. **115**, 235503 (2015).
66. E. D. Palik, *Handbook of Optical Constants of Solids* (Elsevier, 2012).
67. P. B. Johnson and R. W. Christy, "Optical constants of the noble metals," Phys. Rev. B **6**, 4370–4379 (1972).
68. W. Ma, Y. Xu, and B. Xiong, *et al.*, "Pushing the limits of functionality-multiplexing capability in metasurface design based on statistical machine learning," Adv. Mater. **34**, 2110022 (2022).
69. W. Ma, F. Cheng, and Y. Xu, *et al.*, "Probabilistic representation and inverse design of metamaterials based on a deep generative model with semi-supervised learning strategy," Adv. Mater. **31**, 1901111 (2019).
70. J. Y. Yoo, S. Y. Kang, and J. S. Park, *et al.*, "Deep learning for anatomical interpretation of video bronchoscopy images," Sci. Rep. **11**, 23765 (2021).
71. X. Chen, W. Guo, and L. Zhao, *et al.*, "Acute myocardial infarction detection using deep learning-enabled electrocardiograms," Front. Cardiovasc. Med. **8**, 654515 (2021).
72. H. Yu, T. Huang, and B. Feng, *et al.*, "Deep-learning model for predicting the survival of rectal adenocarcinoma patients based on a surveillance, epidemiology, and end results analysis," BMC Cancer **22**, 210 (2022).
73. Y. Zhang, C. Wang, and X. Liu, *et al.*, "Bi-channel compressive hyperspectral imager based on polarization conversion metasurface," Opt. Commun. **549**, 129942 (2023).
74. Q. Song, X. Liu, and C. W. Qiu, *et al.*, "Vectorial metasurface holography," Appl. Phys. Rev. **9**, 011311 (2022).
75. Q. Song, A. Baroni, and R. Sawant, *et al.*, "Ptychography retrieval of fully polarized holograms from geometric-phase metasurfaces," Nat. Commun. **11**, 2651 (2020).
76. F. Ding, B. Chang, and Q. Wei, *et al.*, "Versatile polarization generation and manipulation using dielectric metasurfaces," Laser Photonics Rev. **14**, 2000116 (2020).
77. H. Gao, Y. Wang, and X. Fan, *et al.*, "Dynamic 3D meta-holography in visible range with large frame number and high frame rate," Sci. Adv. **6**, eaba8595 (2020).